Mid-infrared images of β Pictoris and the possible role of planetesimal collisions in the central disk

Charles M. Telesco[1], R. Scott Fisher[2], Mark C. Wyatt[3], Stanley F. Dermott[1], Thomas J. J. Kehoe[1], Steven Novotny[1], Naibi Mariñas[1], James T. Radomski[1], Christopher Packham[1], James De Buizer[4,5] & Thomas L. Hayward[4]

[1]*Department of Astronomy, University of Florida, Gainesville, Florida 32611, USA*
[2]*Gemini Observatory Northern Operations Center, 670 N. A'ohoku Place, Hilo, Hawaii 96720, USA*
[3]*UK Astronomy Technology Centre, Royal Observatory, Edinburgh EH9 3HJ, UK*
[4]*Gemini Observatory Southern Operations Center, c/o AURA, Casilla 603, La Serena, Chile*
[5]*Cerro Tololo Inter-American Observatory, National Optical Astronomy Observatory, Casilla 603, La Serena, Chile*

When viewed in optical starlight scattered by dust, the nearly edge-on debris disk surrounding the A5V star β Pictoris (distance 19.3 pc; ref. 1) extends farther than 1,450 AU from the star[2]. Its large-scale complexity has been well characterized, but the detailed structure of the disk's central ~200-AU region has remained elusive. This region is of special interest, because planets may have formed there during the star's 10–20-million-year lifetime[3,4], perhaps resulting in both the observed tilt of 4.6 degrees relative to the large-scale main disk[5,6] and the partial clearing of the innermost dust[7–9]. A peculiarity of the central disk (also possibly related to the presence of planets) is the asymmetry in the brightness of the 'wings'[9,10], in which the southwestern wing is brighter and more extended at 12 μm than the north-eastern wing. Here we present thermal infrared images of the central disk that imply that the brightness asymmetry results from the presence of a bright clump composed of particles that may differ in size from dust elsewhere in the disk. We suggest that this clump results from the collisional grinding of resonantly trapped planetesimals or the cataclysmic break-up of a planetesimal.

During six nights between UT 2 December 2003 and 3 January 2004, we imaged β Pic at the 8.7-, 11.7-, 12.3-, 18.3- and 24.6-μm regions using the Thermal Region Camera and Spectrograph (T-ReCS), the facility mid-infrared camera on Gemini Observatory's 8-m telescope in Chile. Our mid-infrared images (Fig. 1) show the elongated structure identified previously with emission from dust particles in β Pic's central disk. This 200-AU-sized region coincides with the slightly tilted inner disk identified optically with the Hubble Space Telescope[5]. The central peak coincides with the star, for which the photospheric contribution to the total detected flux density ranges from 3% at 24.6 μm to 71% at 8.7 μm. In the 8.7–18.3-μm images, the SW wing of the disk is noticeably brighter than the NE wing. This mid-infrared asymmetry has been seen at ~12 μm (refs 9–11), and there are previous hints of it at ~18 μm (refs 11, 12). We see it clearly at 18.3 μm, but more significantly our images show a clear trend of decreasing asymmetry with increasing wavelength (Fig. 2). Inseparable from the brightness asymmetry at 11.7, 12.3 and 18.3 μm is a prominent clump centred near SW 52 AU. We estimate the difference in the clump flux density (integrated over an image-resolution element in each unsmoothed image; Table 1) and that of the adjacent minimum at SW 43 AU to be 15, 2 and 7 times the noise at 11.7, 12.3 and 18.3 μm, respectively, in the unsmoothed images. Together these results indicate unambiguously that this feature is real. At 8.7 μm, the feature, if present, is less distinct and perhaps slightly shifted towards the star. The 24.6-μm image shows several clumps, but none corresponds exactly with the one at SW 52 AU. The contrast and positions of those clumps are ambiguous enough (Methods) that we do not consider them further here.

Comparing our results to recent deconvolved Keck images at 17.9 μm (refs 11, 12), we do not confirm at any wavelength the tilted inner feature extending out to roughly ±1″ from the star (see also ref. 13). The resolution (full-width at half-maximum, FWHM) of our 18.3-μm image is 0.54 arcsec, compared to 0.5 arcsec (ref. 11) and 0.7 arcsec (ref. 12) for the original Keck images, and that feature should have been clearly evident in the innermost contours shown in our 18.3-μm image. We do not understand the nature of this discrepancy. Additional imaging can resolve the issue.

Of the several clumps identified by Wahhaj *et al.*[12] in their deconvolved image (with stated resolution twice as good as the observed resolution of 0.7 arcsec), only the one near SW 52 AU, which they designate C′, has a discrete counterpart in our 18.3-μm image. The bright ridge of emission in our image extends to the NE and includes their source C, which we do not see as a discrete source. They[12] do not discuss the statistical significance of the features. To assess this, we consider the strongest source C′, for which their contour levels are 3.6σ at C′ and in the range 2.4–3.0σ for the adjacent minimum 0.8 arcsec to the northeast. If their standard deviation σ applies to the flux within a smoothed resolution element (that is, the 0.7-arcsec-diameter smoothing kernel), the statistical significance of feature C′, as judged by its contrast with the adjacent minimum, is about unity. Because C′ coincides with our source at

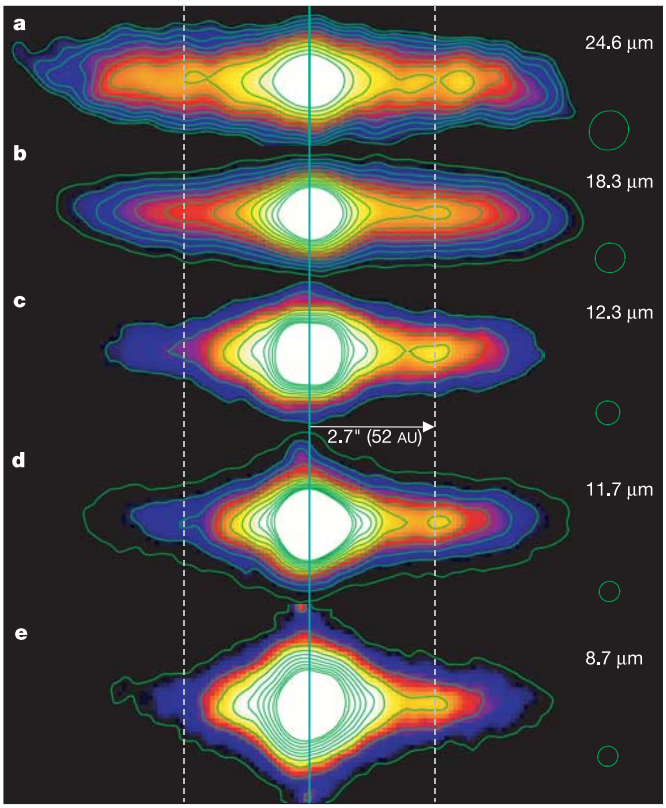

Figure 1 β Pic mid-infrared images. Smoothed images rotated 58° counter-clockwise; NE to left, SW to right, smoothed point-source FWHM contours at right. The vertical solid line is at the star (centre) and the vertical dotted lines are at NE and SW 52 AU. Approximately logarithmic contours (in units of 0.01 mJy pixel^{-1}) are as follows. **a**, 130, 149, 172, 199, 231, 269, 314, 368, 432, 509, 600. **b**, 40, 55, 69, 87, 106, 129, 154, 184, 217, 254, 297, 345, 400. **c**, 18, 30, 44, 55, 77, 96, 118, 142, 169, 200. **d**, 10, 17, 26, 36, 45, 56, 68, 80, 93, 108, 123, 140. **e**, 8, 21, 35, 51, 69, 89, 112, 138, 167, 200. The brightest (inner) colours correspond to the highest-numbered contour levels.

SW 52 AU, our interpretation of their noise characterization may be inaccurate. Nevertheless, we have found in simulations that white noise applied to a uniformly bright, extended source before image smoothing can lead to the appearance of unresolved clumps in the smoothed image resembling those detected in ref. 12.

To probe the nature of the brightness asymmetry, we subtracted the emission in the fainter NW wing from the SW wing at those wavelengths for which we observed an asymmetry (Fig. 3). Most of the resultant residual emission, which has a high signal-to-noise ratio, arises in the projected radial band from 40 to 60 AU, although it is not entirely confined to that region. The distribution is resolved along the major axis at all four wavelengths (resolution elements, Table 1) and is defined by the bright clump at SW 52 AU and a fainter ridge extending out to ~70 AU, both of which seem to be embedded in a fainter component. A point source with peak brightness normalized to the clump peak at 8.7, 11.7, 12.3 and 18.3 μm, respectively, would emit 16, 11, 17 and 15% of the total residual emission between 26 and 113 AU in radius and ±43 AU along the minor axis. The clump appears resolved along the minor (vertical) axis at all wavelengths. At 8–12 μm, the measured minor-axis FWHM values through the clump peak are about twice the smoothed point-spread function (PSF) values (0.4–0.5 arcsec, or 8–10 AU). Quadratic subtraction of the PSF implies intrinsic minor-axis clump widths roughly in the range 13–17 AU. At 18 μm the minor-axis distribution through the clump peak is noticeably asymmetric, with an intrinsic width of about 19 AU. We emphasize that the derived structure and resolution of the clump must be viewed cautiously (and confirmed in detail), because it depends in a complex way on details of the emission on both sides of the disk.

We find that the spectral energy distribution (SED) of the residual emission is noticeably different from that of the NE wing and the central disk as a whole. In contrast to the total wing emission from either side (Fig. 4), for which the flux density increases with wavelength to beyond 25 μm, the SED of the residual peaks shortward of 25 μm. To explore this contrast, we constructed a multi-annulus model for the NE emission wing, assuming it represents part of a disk, with dust particles having an emission efficiency with the generic power-law form $Q_\nu \propto \nu$, where ν is the frequency. The model, based initially only on the 11.7- and 18.3-μm images, indicates that the optical-depth distribution in the NE wing has a maximum at 60–80 AU and a gradual fall-off between 60 and 30 AU (Fig. 5). We identify this central fall-off with the hole inferred previously from the larger-scale SED[7,8] and from 12-μm images with an assumed temperature distribution[9,10]. The NE-wing optical depth drops smoothly by factors of two and three between 70 and 120 AU and 70 and 30 AU, respectively, roughly compatible with the results obtained by Pantin *et al.*[10], who incorporated the brighter SW wing into their models, thereby enhancing the deduced density contrast of the hole. The resultant temperature distribution, which decreases gradually with distance, is much hotter than a blackbody, as expected for small, inefficiently emitting particles[7]. The temperature is ~140 K near NE 52 AU. In contrast, for the same power-law efficiency we estimate the temperature of the clump particles at SW 52 AU to be ~190 K (Fig. 4b). For composite grains composed of silicate and organic refractory material[14], 1-μm-diameter particles at 52 AU can be heated to 140 K, whereas the particles must be five-to-ten times smaller (0.1–0.2 μm) to attain 190 K at that distance. They would also have very high values ($\gg$1) of β, the ratio of radiation and gravitational forces, and so be expelled quickly from the system. Although detailed dust models are needed to explore this issue robustly, the key conclusion based on the relative appearance of the component SEDs is reasonably firm: the particles in the

Table 1 **Observational parameters**

λ (μm)	Δλ (μm)	FWHM (″)	F_ν (Jy)	σ (mJy pixel^{-1})	Δt (s)
8.7	0.8	0.31	2.92	0.032	912
11.7	1.1	0.38	2.72	0.020	2,324
12.3	1.2	0.41	2.72	0.053	912
18.3	1.5	0.54	5.04	0.130	7,298
24.6	2.0	0.72	12.50	0.700	6,604

Pixel size 0.09 arcsec. Array field of view 21″ × 28″. Δλ (μm), filter spectral width at 50% transmission. FWHM, measured full-width at half-maximum intensity of comparison stars, and corresponds to a 'resolution element' referred to in the text. F_ν (Jy), total fluxes integrated over 20″ × 5″ region aligned with disk and centred on star. At 8.7, 11.7, 12.3, 18.3 and 24.6 μm, respectively, peak image brightnesses are 12.4, 17.1, 30.5, 42,3 and 63.9 mJy pixel^{-1}, and stellar photospheric emission is 71, 42, 38, 10 and 3% of tabulated total fluxes. σ (mJy pixel^{-1}), standard deviation for unsmoothed final frames. Δt(s), total time of source photon collection during chop-nod sequence.

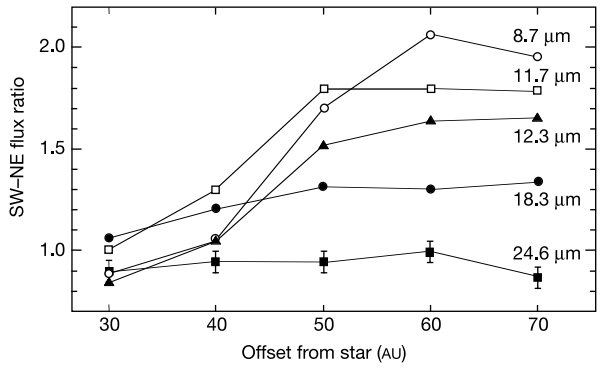

Figure 2 SW flux divided by NE flux versus distance from star. The SW wing is much brighter than the NE wing at shorter wavelengths. At each wavelength, flux densities have been integrated over a strip 10 AU wide along the disk major axis and 97 AU (5 arcsec) along the minor axis and centred on the major axis at the positions where the ratios of the flux densities are plotted. Error bars (1-σ) are as indicated at 24.6 μm and smaller than symbols at other wavelengths.

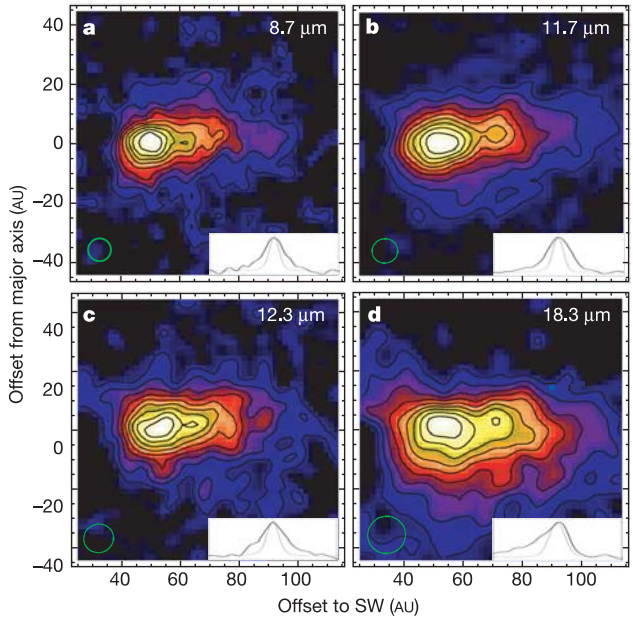

Figure 3 The residual emission. Images result from subtracting the NE wing from the SW wing along lines through the star. The nine evenly spaced contour levels are at the 10, 20, 30, 40, 50, 60, 70, 80 and 90% peak values of 0.228, 0.321, 0.335 and 0.527 mJy pixel^{-1} at 8.7, 11.7, 12.3 and 18.3 μm, respectively. Corresponding peak signal-to-noise ratios are 27, 48, 24 and 15, respectively. The 24.6-μm residual is not shown, because features are ambiguous. PSF FWHM contours are in the lower left corners. Each inset shows a minor-axis scan (with the displayed linear scale compressed by a factor of two) through the peak (NW to right, SE to left) and the normalized PSF.

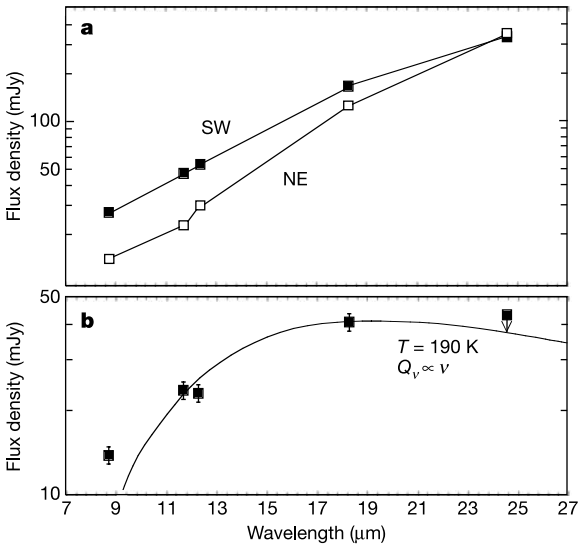

Figure 4 Disk spectral energy distributions. **a**, SEDs of NE and SW wings. Flux densities are total values in a 1-arcsec-diameter circle centred at NE and SW 52 AU along the disk's major axis from the star. Symbol sizes indicate magnitudes of flux uncertainties, primarily due to uncertainties in photometric calibration (±10%). **b**, SED of residual emission based on SEDs. Uncertainties as in **a**. The upper limit at 24.6 μm is 3σ. The curve is $Q_\nu B_\nu(T)$, normalized to the 11.7- and 18.3-μm flux densities, where the assumed particle emission efficiency follows the relation $Q_\nu \propto \nu$ and the particle temperature has the value $T = 190$ K.

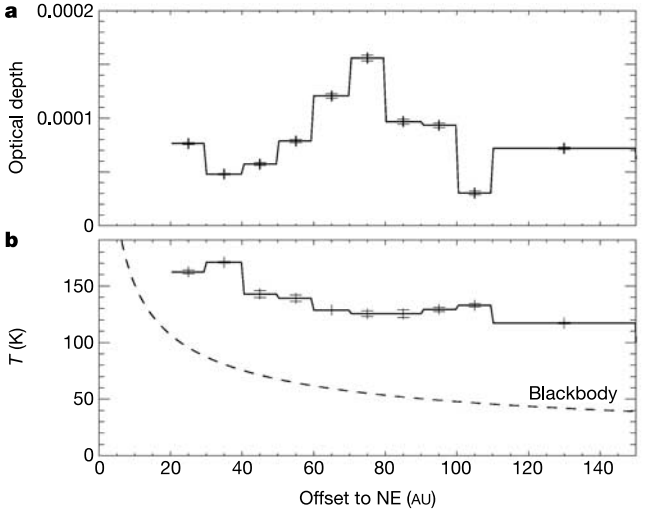

Figure 5 Model distributions for the NE side of disk. **a**, **b**, Face-on optical depth (**a**), and temperature of dust particles (**b**) emitting the 11.7- and 18.3-μm emission, both computed assuming $Q_\nu \propto \nu$. The expected blackbody temperature distribution (dashed line in **b**) is shown for comparison. Because of the presence of silicate-feature emission and uncertainties in the PSF, the modelling is uncertain for locations within 20 AU of the star, and those results are not shown.

vicinity of the clump at SW 52 AU differ in temperature, size and/or composition from the dust elsewhere in the disk.

The clump particles may have distinct, detectable spectroscopic signatures. Recent mid-infrared spectroscopy indicates an asymmetric distribution of sub-micrometre glassy olivine grains emitting within 30 AU of the star[13], which is much closer to the star than the clump region. The possible relationship of these components has yet to be explored, but the lower inferred temperatures of the clump particles (<200 K) compared to those inner particles (>300 K; ref. 13) suggests that the silicate feature, if emitted by the clump particles, would probably be at least one to two orders of magnitude weaker than that seen closer to the star.

There are several mechanisms that produce a selective enhancement or diminishment of particles with certain ranges of size, shape or composition that can lead to a spatially localized, visually prominent inhomogeneity in the dust population of a disk. If planets are present in a debris disk, the inward migration of dust particles due to Poynting–Robertson drag can lead to resonant trapping[15–17], which produces localized structure sensitive to the physical properties of the particles. However, those disks are relatively tenuous, in contrast to the higher-density β Pic disk, where the particles are expected to be destroyed by mutual collisions on timescales too short for them to experience significant Poynting–Robertson drag[18]. Another possibility is that the very small particles that we observe in the β Pic clump are produced by ongoing, grinding collisions among a planetesimal population itself trapped in planetary resonances[15,19], which has the appealing attribute that the resultant clumps are quasi-permanent and thus more likely to be observable. However, in view of the relatively young age of the β Pic system and the evidence of orbital dynamism there[20,21], we emphasize the alternative possibility that the catastrophic collisional break-up of a large planetesimal has released a distinct, spatially asymmetric population of particles into the disk. This distinct population, we speculate, might have a size distribution favouring particles smaller than those more widely distributed in the disk[22]. We estimate the total mass of the mid-infrared-emitting clump particles (density, 1 g cm^{-3}) to be 4×10^{20} g, which would constitute a spherical parent body around 100 km in diameter. Depending on the size distribution of collision fragments, the parent body could be substantially larger than this. Because they are blown out of the system quickly, this collision would have occurred within a fraction of the orbital period of 270 yr, unless blow-out is substantially inhibited by gas drag[23]. Fragment post-collision velocities of ~1–2 km s^{-1} could account for the bright clump's tentatively identified vertical size of ~10–20 AU if the collisional break-up occurred 50 yr ago. That timescale is also commensurate with radiation-pressure-driven dispersal from the clump peak of high-β, submicrometre-sized debris particles at typically 4–6 km s^{-1} to account for the ~40-AU radial extent of the residual distribution (Fig. 3). The probability of observing such an event is low[22,24], but we do know that during the late stages of planet formation in the Solar System, violent, catastrophic collisions must have been common; such collisions have even been suggested to account for the origin of the Moon[25] and structures in the zodiacal cloud[26]. A similar event in the β Pic debris disk would result in its flaring into visibility, perhaps as we see it today and in accord with recent suggestions[26,27] that catastrophic collisions must lead to just such dramatic observable consequences. □

Methods

Observational procedure

We used standard chop-nod techniques at the Gemini South telescope with a 15-arcsec chop throw orthogonal to the disk's major axis. The PSF at 8.7–18.3 μm was determined from the K1 III star PPM 335509 (HR 2553) located ~10° from β Pic. We used the standard γ Reticulum to determine the PSF at 24.6 μm. At each wavelength the observation sequence consisted of imaging the PSF star, then β Pic, then the PSF star. The final images at 11.7, 18.3 and 24.6 μm were formed from registered stacks of five, seven and seven individual images, respectively. Between each exposure within a stack, the telescope was offset ('dithered') approximately 1 arcsec. The images at 8.7 and 12.3 μm were each obtained as a single on-source exposure. Some artefacts are apparent: the bright spots, due to previously known detector cross-talk, 2.5 arcsec above and below the main peak at 8.8 μm, and the optical ghost 2 arcsec above the peak at 11.7 μm. Previous mid-infrared imaging of β Pic indicates that the major axis of the central disk is oriented at position angle 33°. To minimize the introduction of any spurious features due to row- or column-correlated pattern structure known to be associated with this detector device, while also allowing for the possibility of detecting extended emission along the major axis at 11.7, 18.3 and 24.6 μm, T-ReCS was rotated so that the disk's major axis was oriented diagonally on the array. At 8.7 and 12.3 μm the disk's major axis was oriented vertically (that is, along a 240-pixel-long column) on the detector array. The sky was clear during all observations,

and all images were made at airmasses less than 1.2 with Gemini facility guiding and tip-tilt engaged. To improve the signal-to-noise ratio, the images displayed in Fig. 1 have been smoothed with gaussians of FWHM of 0.223, 0.223, 0.267, 0.356 and 0.445 arcsec at 8.7, 11.7, 12.3, 18.3 and 24.6 μm, respectively.

The probability that the SW 52 AU clump is a chance superposition of an unrelated background object is negligibly small ($<4 \times 10^{-5}$), as determined elsewhere[28] for a source of comparable brightness. Regarding the clumps apparent in the 24.6-μm image, we estimate the contrast of the brightest clump at SW 60 AU with the adjacent inner minimum to be approximately three times the noise, but the centroid of that clump is separated from the minimum (SW 52 AU) by less than the 24.6-μm resolution of 14 AU (Table 1). Thus, we make no firm judgement about the reality of the 24.6-μm clumps, ignoring for now the detailed 24.6-μm structure. We note that, if ultimately confirmed, it could provide significant additional insight into disk processes.

Dust mass and models

To characterize the NE disk emission, we considered a single population of dust grains with the commonly used approximation that the emission efficiency Q_ν is proportional to frequency. Other forms for Q_ν basically raise or lower the temperature and optical depth distributions, but our purpose, which is to contrast the dust properties in the NE and SW wings, is well served by our simple assumption. The assumed value for the stellar luminosity is $8.7L_\odot$, where $L_\odot$ is the luminosity of the Sun. The model disk extends out to 150 AU and is composed of 11 annuli that are 10 AU wide in the 0–110 AU region and one annulus that is 40 AU wide in the 110–150-AU region. We ignore results for the region within 20 AU of the star because of the contribution of the silicate feature and uncertainties in the PSF. Each annulus is assumed to be uniform in temperature and density. The modelling computes the distributions of temperature and face-on optical depth for the annuli that give rise to the brightness distributions observed at 11.7 and 18.3 μm. The models incorporate an inclination of the whole disk to the line of sight and opening angles as free parameters for each annulus. Optical depths and temperatures of the annuli were used to determine the flux in the appropriate wavebands emitted by the portion of the disk in a narrow radial range. The model is three-dimensional, with flux spread evenly in both latitude (in the range allowed by the disk opening angle) and longitude. The disk observations were simulated with the flux from the model being integrated along the line of sight of each pixel. The point-like stellar flux was then included at the centre. The image was then convolved with the PSF observed at the appropriate wavelength and additional smoothing added at the same level applied for the displayed images. The modelling procedure started with initial values for the annuli, then the parameters for each annulus were improved in turn by considering how varying them affected the resulting image. This procedure worked from the outermost to the innermost annulus and was repeated until the parameters converged. Uncertainties in the derived parameters were determined from the pixel-to-pixel deviation in the observation. A detailed description of the modelling for β Pic will be presented elsewhere by M.C.W. and co-workers.

Received 14 September; accepted 2 December 2004; doi:10.1038/nature03255.

1. Crifo, F., Vidal-Madjar, A., Lallement, R., Ferlet, R. & Gerbaldi, M. β Pictoris revisited by Hipparcos. Star properties. *Astron. Astrophys.* **320,** L29–L32 (1997).
2. Larwood, J. D. & Kalas, P. G. Close stellar encounters with planetesimal disks: the dynamics of asymmetry in the β Pictoris system. *Mon. Not. R. Astron. Soc.* **323,** 402–416 (2001).
3. Barrado y Navascués, D., Stauffer, J. R., Song, I. & Caillault, J.-P. The age of Beta Pictoris. *Astrophys. J.* **520,** L123–L126 (1999).
4. Zuckerman, B., Song, I., Bessell, M. S. & Webb, R. A. The β Pictoris moving group. *Astrophys. J.* **562,** L87–L90 (2001).
5. Heap, S. *et al.* Space telescope imaging spectrograph coronagraphic observations of β Pictoris. *Astrophys. J.* **539,** 435–444 (2000).
6. Mouillet, D., Larwood, J. D., Papaloizou, J. C. B. & Lagrange, A. M. A planet on an inclined orbit as an explanation of the warp in the β Pictoris disc. *Mon. Not. R. Astron. Soc.* **292,** 896–904 (1997).
7. Telesco, C. M., Becklin, E. E., Wolstencroft, R. D. & Decher, R. Resolution of the circumstellar disk of β Pictoris at 10 and 20 μm. *Nature* **335,** 51–53 (1988).
8. Backman, D. E., Gillett, F. C. & Witteborn, F. C. Infrared observations and thermal models of the β Pictoris dust disk. *Astrophys. J.* **385,** 670–679 (1992).
9. Lagage, P. O. & Pantin, E. Dust depletion in the inner disk of Beta Pictoris as a possible indicator of planets. *Nature* **369,** 628–630 (1994).
10. Pantin, E., Lagage, P. O. & Artymowicz, P. Mid-infrared images and models of the β Pictoris dust disk. *Astron. Astrophys.* **327,** 1123–1136 (1997).
11. Weinberger, A. J., Becklin, E. E. & Zuckerman, B. The first spatially resolved mid-infrared spectroscopy of β Pictoris. *Astrophys. J.* **584,** L33–L37 (2003).
12. Wahhaj, Z. *et al.* The inner rings of β Pictoris. *Astrophys. J.* **584,** L27–L31 (2003).
13. Okamoto, Y. K. *et al.* An extrasolar planetary system revealed by planetesimal belts in β Pictoris. *Nature* **431,** 660–662 (2004).
14. Li, A. & Greenberg, J. M. A comet dust model for the β Pictoris disk. *Astron. Astrophys.* **331,** 291–313 (1998).
15. Ozernoy, L. M., Gorkavyi, N. N., Mather, J. C. & Taidakova, T. A. Signatures of exosolar planets in dust disks. *Astrophys. J.* **537,** L147–L151 (2000).
16. Sicardy, B., Beaugé, C., Ferraz-Mello, S., Lazzaro, D. & Roques, F. Capture of grains into resonances through Poynting-Robertson drag. *Celest. Mech. Dyn. Astron.* **57,** 373–390 (1993).
17. Dermott, S. F., Jayaraman, S., Xu, Y. L., Gustafson, B. & Liou, J. C. A circumsolar ring of asteroidal dust in resonant lock with the Earth. *Nature* **369,** 719–723 (1994).
18. Wyatt, M. C. *et al.* How observations of circumstellar disk asymmetries can reveal hidden planets: pericenter glow and its application to the HR4796 disk. *Astrophys. J.* **527,** 918–944 (1999).
19. Wyatt, M. C. Resonant trapping of planetesimals by planet migration: debris disk clumps and Vega's similarity to the Solar System. *Astrophys. J.* **598,** 1321–1340 (2003).
20. Lagrange-Henri, A. M., Vidal-Madjar, A. & Ferlet, R. The β Pictoris circumstellar disk. VI. Evidence for material falling on to the star. *Astron. Astrophys.* **190,** 275–282 (1988).
21. Beust, H., Vidal-Madjar, A., Ferlat, R. & Lagrange-Henri, A. M. Cometary-like bodies in the protoplanetary disk around β Pictoris. *Astrophys. Space Sci.* **212,** 147–157 (1994).
22. Wyatt, M. C. & Dent, W. R. F. Collisional processes in extrasolar planetesimal discs—dust clumps in Fomalhaut's debris disc. *Mon. Not. R. Astron. Soc.* **334,** 589–607 (2002).
23. Brandeker, A., Liseau, R., Olofsson, G. & Fridlund, M. The spatial structure of the β Pictoris gas disk. *Astron. Astrophys.* **413,** 681–691 (2004).
24. Dominik, C. & Decin, G. Age dependence of the Vega phenomenon: theory. *Astrophys. J.* **598,** 626–635 (2003).
25. Hartmann, W. K. & Davis, D. R. Satellite-sized planetesimals and lunar origin. *Icarus* **24,** 504–515 (1975).
26. Dermott, S. F., Kehoe, T. J. J., Durda, D. D., Grogan, K. & Nesvorný, D. in *Asteroids, Comets, and Meteors 2002* (ed. Warmbein, B.) ESA SP-500, 319–322 (Publications Division, Noordwijk, 2002).
27. Kenyon, S. J. & Bromley, B. C. Detecting the dusty debris of terrestrial planet formation. *Astrophys. J.* **602,** L133–L136 (2004).
28. Van Paradijs, J., Telesco, C. M., Kouveliotou, C. & Fishman, G. J. 10 micron detection of the hard x-ray transient GRO J0422+32: free-free emission from an x-ray-driven accretion disk wind? *Astrophys. J.* **429,** L19–L23 (1994).

Acknowledgements We dedicate this paper to the memory of our colleague F. Gillett, infrared astronomy pioneer and co-discoverer of circumstellar debris disks. We thank K. Hanna, J. Julian and R. Piña for contributions to the success of T-ReCS; F. Varosi for assistance with data reduction; the Gemini Observatory staff in Chile, particularly M.-C. Hainaut-Rouelle, for technical assistance; and D. Simons of Gemini Observatory for support. This paper is based on observations (programme number GS-2003B-14) obtained at the Gemini Observatory, which is operated by the Association of Universities for Research in Astronomy, Inc., under a cooperative agreement with the NSF on behalf of the Gemini partnership: the National Science Foundation (United States), the Particle Physics and Astronomy Research Council (United Kingdom), the National Research Council (Canada), CONICYT (Chile), the Australian Research Council (Australia), CNPq (Brazil) and CONICET (Argentina). This research was funded in part by an NSF grant to C.M.T.

Competing interests statement The authors declare that they have no competing financial interests.

Correspondence and requests for materials should be addressed to C.M.T. (telesco@astro.ufl.edu).

Revised rates for the stellar triple-α process from measurement of ^{12}C nuclear resonances

Hans O. U. Fynbo[1], Christian Aa. Diget[1], Uffe C. Bergmann[2], Maria J. G. Borge[3], Joakim Cederkäll[2], Peter Dendooven[4], Luis M. Fraile[2], Serge Franchoo[2], Valentin N. Fedosseev[2], Brian R. Fulton[5], Wenxue Huang[6], Jussi Huikari[6], Henrik B. Jeppesen[1], Ari S. Jokinen[6,7], Peter Jones[6], Björn Jonson[8], Ulli Köster[2], Karlheinz Langanke[1], Mikael Meister[8], Thomas Nilsson[2], Göran Nyman[8], Yolanda Prezado[3], Karsten Riisager[1], Sami Rinta-Antila[6], Olof Tengblad[3], Manuela Turrion[3], Youbao Wang[6], Leonid Weissman[2], Katarina Wilhelmsen[8], Juha Äystö[6,7] & The ISOLDE Collaboration[2]

[1]*Department of Physics and Astronomy, University of Aarhus, 8000 Århus C, Denmark*
[2]*CERN, CH-1211 Geneva 23, Switzerland*
[3]*Instituto Estructura de la Materia, CSIC, Serrano 113bis, E-28006, Madrid, Spain*
[4]*KVI, Zernikelaan, 9747 AA Groningen, The Netherlands*
[5]*Department of Physics, University of York, Heslington, YO10 5DD, UK*
[6]*Department of Physics, University of Jyväskylä, FIN-40351 Jyväskylä, Finland*
[7]*Helsinki Institute of Physics, FIN-00014 University of Helsinki, Finland*
[8]*Experimental Physics, Chalmers University of Technology and Göteborg University, S-41296 Göteborg, Sweden*

In the centres of stars where the temperature is high enough, three α-particles (helium nuclei) are able to combine to form ^{12}C because of a resonant reaction leading to a nuclear excited state[1]. (Stars with masses greater than ~0.5 times that of the Sun will at some point in their lives have a central temperature high enough for this reaction to proceed.) Although the reaction rate is of critical significance for determining elemental abundances in the